



Article

Facile Synthesis of 2D/2D $\text{Ti}_2\text{C}_3/\text{ZnIn}_2\text{S}_4$ Heterostructure for Enhanced Photocatalytic Hydrogen Generation

Yongjuan Chen, Yanfang Ge, Chunling Wu, Hua Tang, Xiu Luo, Jiao He , Liang Jiang, Zhiying Yan and Jiaqiang Wang *

School of Chemical Sciences & Technology, Yunnan Province Engineering Research Center of Photocatalytic Treatment of Industrial Wastewater, School of Materials and Energy, Yunnan University, Kunming 650091, China
* Correspondence: jqwang@ynu.edu.cn; Tel.: +86-871-65031567

Abstract: ZnIn_2S_4 , a novel two-dimensional visible light-responsive photocatalyst, has attracted much attention in the photocatalytic evolution of H_2 under visible light irradiation due to its attractive intrinsic photoelectric properties and geometric configuration. However, ZnIn_2S_4 still has severe charge recombination, which results in moderate photocatalytic performance. Herein, we report the successful synthesis of 2D/2D $\text{ZnIn}_2\text{S}_4/\text{Ti}_3\text{C}_2$ nanocomposites by a facile one-step hydrothermal method. The efficiency of the nanocomposites in photocatalytic hydrogen evolution under visible light irradiation was also evaluated for different ratios of Ti_3C_2 , and the optimal photocatalytic activity was achieved at 5% Ti_3C_2 . Importantly, the activity was significantly higher than that of pure ZnIn_2S_4 , $\text{ZnIn}_2\text{S}_4/\text{Pt}$, and $\text{ZnIn}_2\text{S}_4/\text{graphene}$. The enhanced photocatalytic activity is mainly due to the close interfacial contact between Ti_3C_2 and ZnIn_2S_4 nanosheets, which amplifies the transport of photogenerated electrons and enhances the separation of photogenerated carriers. This research describes a novel approach for the synthesis of 2D MXenes for photocatalytic hydrogen production and expands the utility of MXene composite materials in the fields of energy storage and conversion.

Keywords: ZnIn_2S_4 ; MXene; Ti_2C_3 ; photocatalytic; hydrogen generation



Citation: Chen, Y.; Ge, Y.; Wu, C.; Tang, H.; Luo, X.; He, J.; Jiang, L.; Yan, Z.; Wang, J. Facile Synthesis of 2D/2D $\text{Ti}_2\text{C}_3/\text{ZnIn}_2\text{S}_4$ Heterostructure for Enhanced Photocatalytic Hydrogen Generation. *Int. J. Mol. Sci.* **2023**, *24*, 3936. <https://doi.org/10.3390/ijms24043936>

Academic Editor: Shunfang Li

Received: 2 February 2023

Revised: 10 February 2023

Accepted: 13 February 2023

Published: 15 February 2023



Copyright: © 2023 by the authors. Licensee MDPI, Basel, Switzerland. This article is an open access article distributed under the terms and conditions of the Creative Commons Attribution (CC BY) license (<https://creativecommons.org/licenses/by/4.0/>).

1. Introduction

As a kind of sustainable clean energy, hydrogen energy has great application potential in solving the problem of energy shortage. Fujishima and Honda were the first to split water into H_2 and O_2 via a titania (TiO_2) electrode in 1972 [1]. Since then, semiconductor photocatalytic hydrogen production has been purposefully pursued due to its potential applications in the production of clean hydrogen energy [2,3]. However, the application of photocatalysis is limited by the absorption of sunlight, the efficiency of charge separation, and the interfacial catalytic reaction [4].

One strategy to improve the photocatalytic activity is through the development and use of two-dimensional (2D) nanocrystallization of semiconductor photocatalytic materials. These materials offer larger specific surface area with more active sites, while the ultra-thin nano layer can shorten the carrier transport distance and facilitate its migration to the catalyst surface. ZnIn_2S_4 is a promising photocatalytic H_2 generation photocatalyst due to its desirable band gap in the visible light region [5,6]. In general, ZnIn_2S_4 shows two different crystal phases of hexagonal lattice and cubic lattice. A large number of previous reports indicated that hexagonal phases had better stability and higher photocatalytic activity. Most often, flake structures have been observed in the morphology of hexagonal ZnIn_2S_4 due to the stacking of S-Zn-S-In-S-In-S layers [7–10]. Advantageously, the unique structure of 2D ZnIn_2S_4 nanosheets decreases the diffusion distance of electrons and improves the separation of photoinduced charges, while a large number of exposed surface atoms can provide rich active sites [11].

However, due to the low separation efficiency and migration capacity of photoexcited charge carriers, the photocatalytic activity of pure ZnIn_2S_4 is insufficient [12,13]. Over the

years, numerous efforts have been made to improve ZnIn_2S_4 , such as doping with metal ions [14,15], combination with semiconductor [16], construction of heterojunction [17], coupling cocatalyst [18], etc. The construction of 2D/2D heterostructures can form more charge transfer channels, which is conducive to the spatial separation and migration of carriers [19,20]. Therefore, the assembly of new heterostructures is considered an effective strategy to improve the photocatalytic performance of ZnIn_2S_4 .

Ti_3C_2 MXene, as a new 2D material, has attracted extensive attention in photocatalysis because of its special metallic conductivity. Ti_3C_2 is rich in hydrophilic functional groups (-OH, -O, -F) on the surface, which is favorable for composites with semiconductor photocatalytic materials. A sufficiently positive Fermi level (0.71 eV vs. NHE) of Ti_3C_2 is conducive to the transfer of photoelectrons from semiconductors to Ti_3C_2 , as well as the effective separation of electron-hole pairs. Recently, it has been reported that ZnIn_2S_4 nanosheets were grown in situ on Ti_3C_2 nanosheets to form a sandwich-like hierarchical heterostructure [21]. The unique hierarchical structure confers the system with superior photoexcited charge transport ability, which further accelerates photoexcited charge separation.

In this study, 2D/2D $\text{ZnIn}_2\text{S}_4/\text{Ti}_3\text{C}_2$ nanocomposites were successfully prepared by a simple one-step hydrothermal method, and the photocatalytic performance of the composites with different ratios of Ti_3C_2 was evaluated in the visible light region. The photocatalytic activity reached the maximum for a mass ratio of 5% Ti_3C_2 , and it was significantly higher than that of pure ZnIn_2S_4 , $\text{ZnIn}_2\text{S}_4/\text{Pt}$, and $\text{ZnIn}_2\text{S}_4/\text{graphene}$. The enhanced photocatalytic activity is mainly due to the close interfacial contact between Ti_3C_2 and ZnIn_2S_4 nanosheets, which accelerates the transport of photoelectrons and increases the separation of photogenerated carriers.

2. Results

2.1. Characterizations

XRD was used to determine the crystalline phases of the samples, as shown in Figure 1. Notably, the largest diffraction peak for the (104) plane of Ti_3AlC_2 , which was at 39.0° , disappeared after HF treatment, indicating the removal of Al layers of Ti_3AlC_2 [22]. In addition, the diffraction peaks of the (002) plane at 9.4° and the (004) plane at 19.1° shifted to lower degrees and become broader, which was ascribed to increase in the interlayer spacing of Ti_3C_2 [23]. This can also be evidenced by SEM images of Ti_3C_2 (Figure 2b). Compared with Ti_3AlC_2 (Figure 2a), Ti_3C_2 has an obviously layered microstructure. These results confirmed the successful transformation of Ti_3AlC_2 into layered Ti_3C_2 .

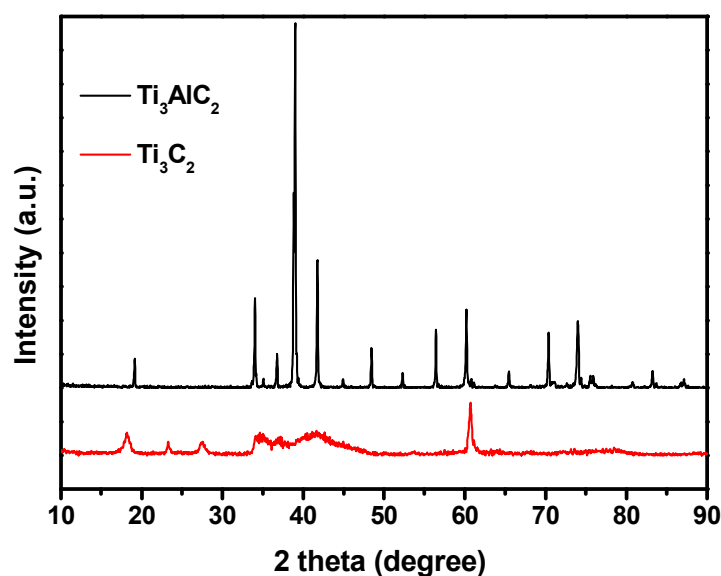


Figure 1. XRD patterns for Ti_3AlC_2 and obtained Ti_3C_2 by etching the Al layer of Ti_3AlC_2 with HF solution.

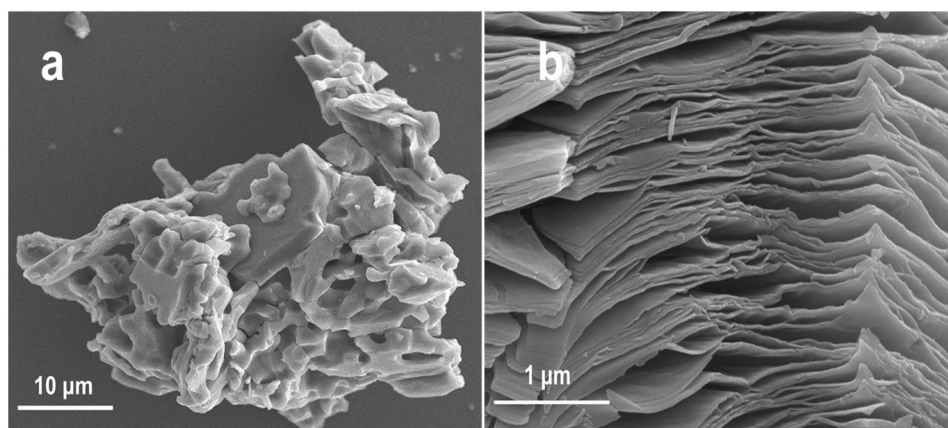


Figure 2. SEM images of (a) Ti_3AlC_2 and (b) obtained Ti_3C_2 by etching the Al layer of Ti_3AlC_2 with HF solution.

$\text{ZnIn}_2\text{S}_4/\text{Ti}_3\text{C}_2$ nanocomposites were synthesized via a facile one-step hydrothermal method. The mass ratio of ZnIn_2S_4 to Ti_3C_2 was varied to determine the optimal composition, and mass ratios of 2 wt.%, 5 wt.%, 10 wt.%, 20 wt.%, and 50 wt.% corresponded to samples ZIST-2, ZIST-5, ZIST-10, ZIST-20, and ZIST-50, respectively. Figure 3 presents the XRD patterns of $\text{ZnIn}_2\text{S}_4/\text{Ti}_3\text{C}_2$ composites with different Ti_3C_2 content, and the $\text{ZnIn}_2\text{S}_4/\text{Ti}_3\text{C}_2$ composites had similar diffraction peaks to that of hexagonal ZnIn_2S_4 [18]. In addition, no obvious diffraction peaks of Ti_3C_2 were found in the XRD patterns of the composites, indicating the limited amount and weak diffraction intensity of Ti_3C_2 . Meanwhile, no diffraction peak of TiO_2 was found, which suggested Ti_3C_2 will not transform into TiO_2 at 150 °C. Therefore, the temperature for sample synthesis is feasible in this work.

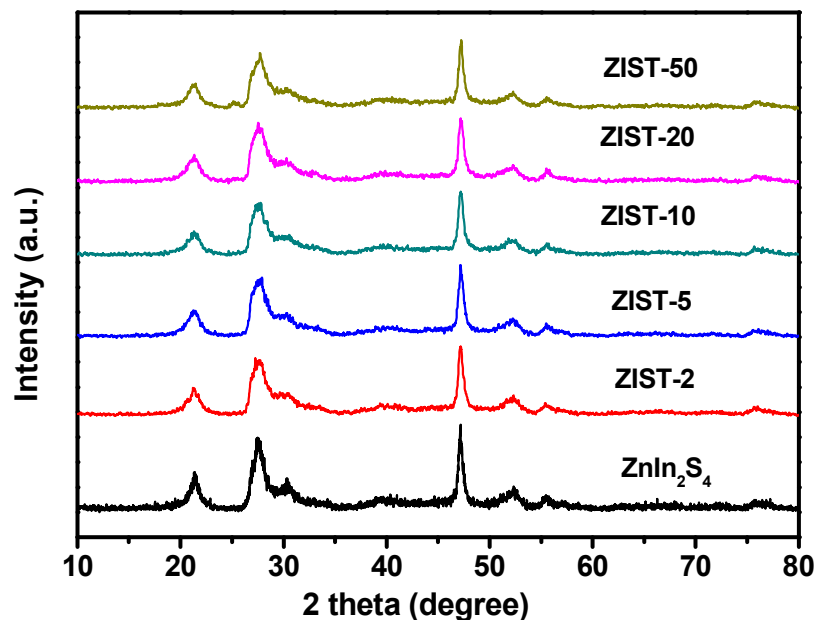


Figure 3. XRD patterns of $\text{ZnIn}_2\text{S}_4/\text{Ti}_3\text{C}_2$ composites with different Ti_3C_2 content.

SEM and TEM were used to observe the morphologies of the samples. The pure ZnIn_2S_4 had a 3D hierarchical flower-like structure self-assembled by 2D nanosheets (Figure 4) according to previous reports [24,25]. The SEM images of $\text{ZnIn}_2\text{S}_4/\text{Ti}_3\text{C}_2$ composites (ZIST-5) showed ultrathin nanosheets of ZnIn_2S_4 densely populating the surface of the layered Ti_3C_2 (Figure 5a). It can be clearly observed that ZnIn_2S_4 is an outer layer closely attached to the surface Ti_3C_2 , which is the inner layer in Figure 5b. Ti_3C_2 retains an integrated lamellar structure in the TEM images (Figure 5c) of $\text{ZnIn}_2\text{S}_4/\text{Ti}_3\text{C}_2$. Lattice spacing of 0.32 nm and lattice

fringes of 0.26 nm were determined in the HRTEM image of $\text{ZnIn}_2\text{S}_4/\text{Ti}_3\text{C}_2$, corresponding to the (102) plane of hexagonal ZnIn_2S_4 [18] and the (010) plane of Ti_3C_2 , respectively [26]. These results indicate that ZnIn_2S_4 nanosheets were anchored on Ti_3C_2 rather than simply mixed.

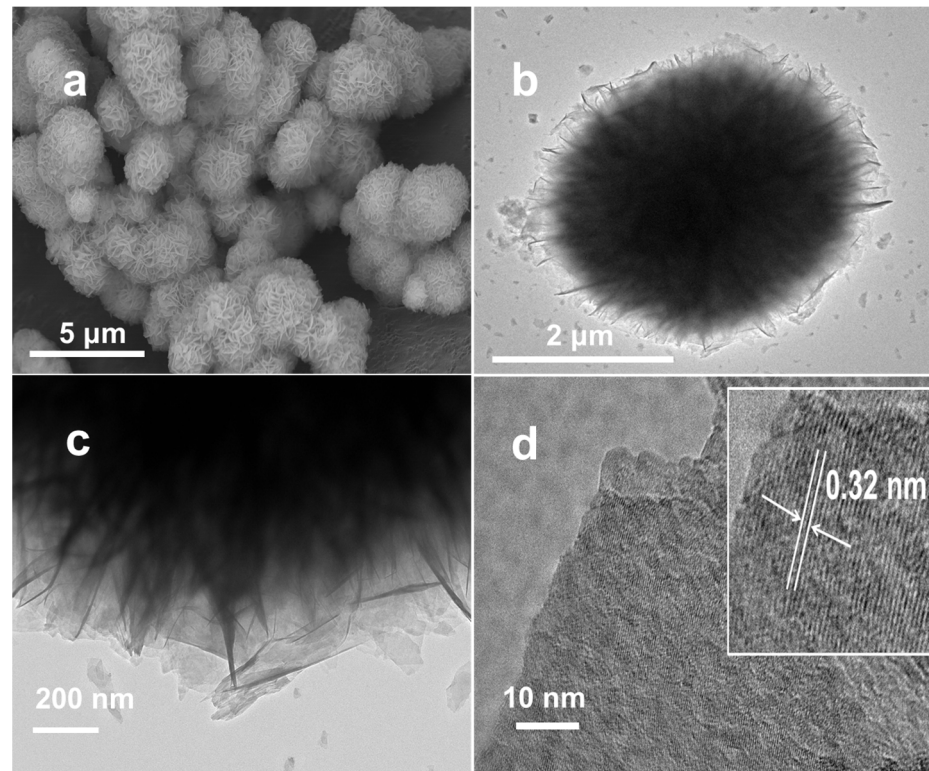


Figure 4. (a) Typical SEM and (b,c) TEM images of ZnIn_2S_4 at different magnifications, (d) and HRTEM image of ZnIn_2S_4 nanocrystallinity.

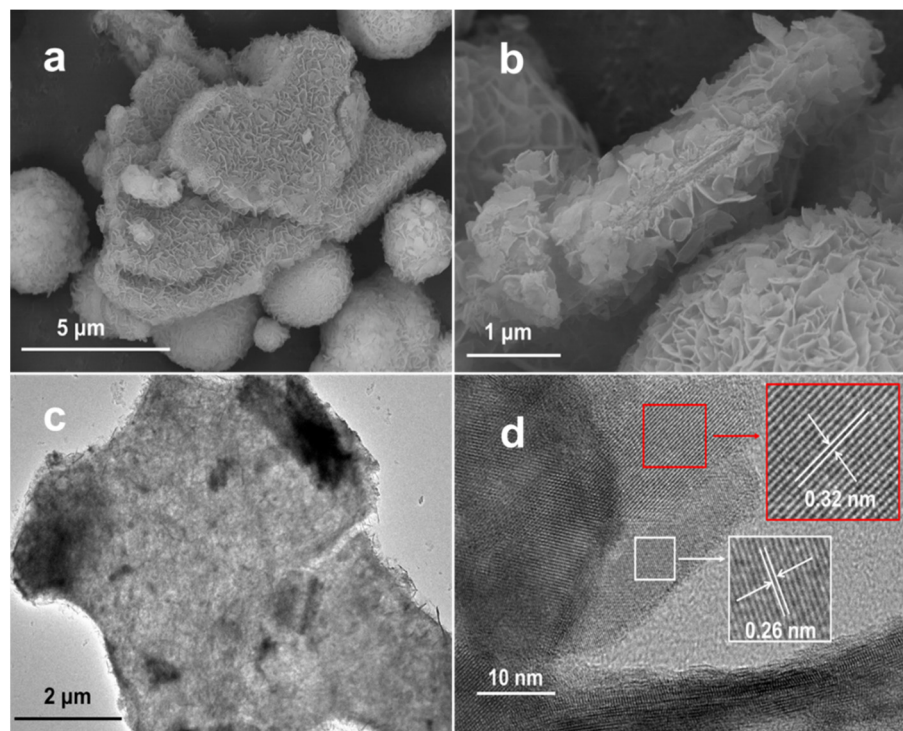


Figure 5. SEM images (a,b), (c) TEM, and (d) HRTEM images of $\text{ZnIn}_2\text{S}_4/\text{Ti}_3\text{C}_2$ composites (ZIST-5).

Next, the surface chemistry of the photocatalyst was investigated by XPS. As shown in Figure 6, a weak signal was observed in the Ti 2p spectrum of ZIST-5, which is mainly due to the existence of Ti_3C_2 in the inner layer of the sample and its content is too low. With the increase in Ti_3C_2 content, the Ti 2p signal becomes stronger. When the mass ratio of Ti_3C_2 reaches 50% of ZnIn_2S_4 (ZIST-50), four peaks at 454.9, 459.2, 461.8, and 464.8 eV were observed in the Ti 2p spectrum, correlating with Ti-O 2p_{1/2}, Ti-C 2p_{1/2}, Ti-O 2p_{3/2}, and Ti-C 2p_{3/2}, respectively [27]. Ti-O is unlikely to be attributable to TiO_2 , because it can be seen from XRD that Ti_3C_2 will not transform into TiO_2 under the reaction conditions of preparing $\text{ZnIn}_2\text{S}_4/\text{Ti}_3\text{C}_2$. Ti-O is formed during the preparation of Ti_3C_2 due to the substitution of O or OH for Tx in $\text{Ti}_3\text{C}_2\text{Tx}$ [28]. Consistent with the Ti 2p spectrum, the C1s peak at 281.6 eV was assigned to Ti-C, and its intensity increased with increasing Ti_3C_2 content (Figure 7). Moreover, compared with pure ZnIn_2S_4 , the Zn 2p and In 3d peaks in the XPS spectra of $\text{ZnIn}_2\text{S}_4/\text{Ti}_3\text{C}_2$ shifted towards higher binding energies, while the S 2p peak shifted to lower binding energy. These changes suggest a strong electronic interaction between Ti_3C_2 and ZnIn_2S_4 (Figures 8–10).

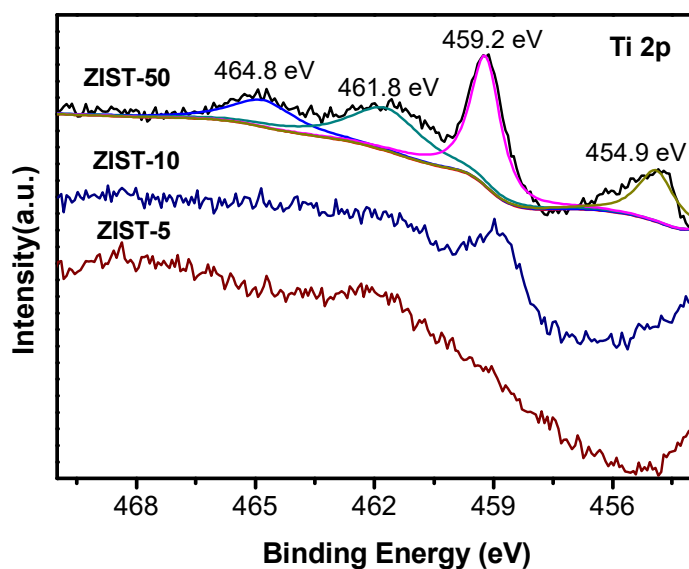


Figure 6. XPS Ti 2p spectra of $\text{ZnIn}_2\text{S}_4/\text{Ti}_3\text{C}_2$ composites with different Ti_3C_2 content.

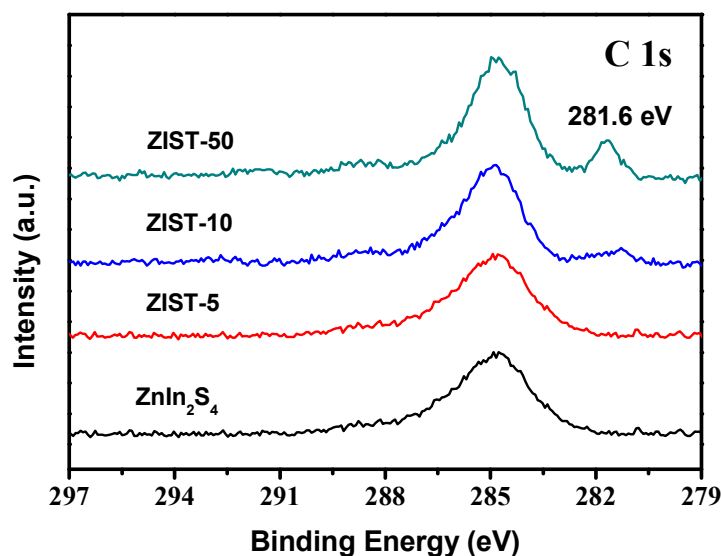


Figure 7. XPS C 1s spectra of ZnIn_2S_4 and $\text{ZnIn}_2\text{S}_4/\text{Ti}_3\text{C}_2$ composites with different Ti_3C_2 content.

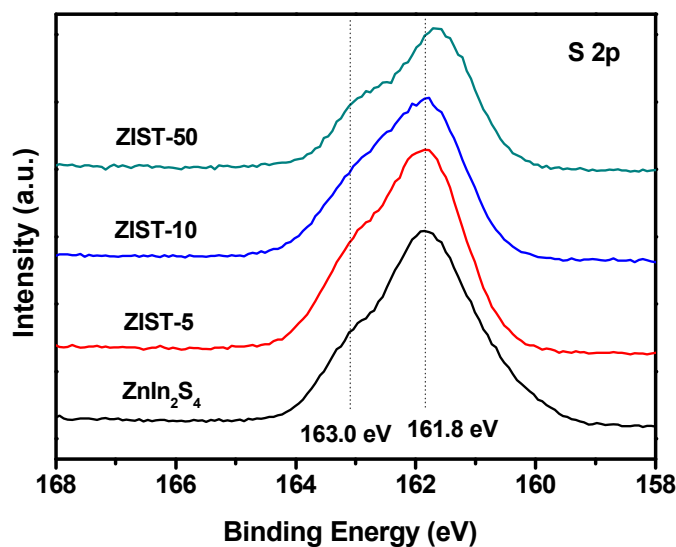


Figure 8. XPS S 2p spectra of ZnIn₂S₄ and ZnIn₂S₄/Ti₃C₂ composites with different Ti₃C₂ content.

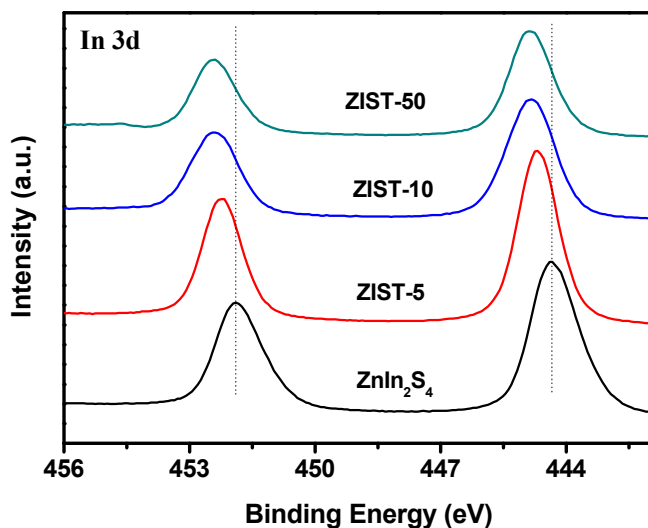


Figure 9. XPS In 3d spectra of ZnIn₂S₄ and ZnIn₂S₄/Ti₃C₂ composites with different Ti₃C₂ content.

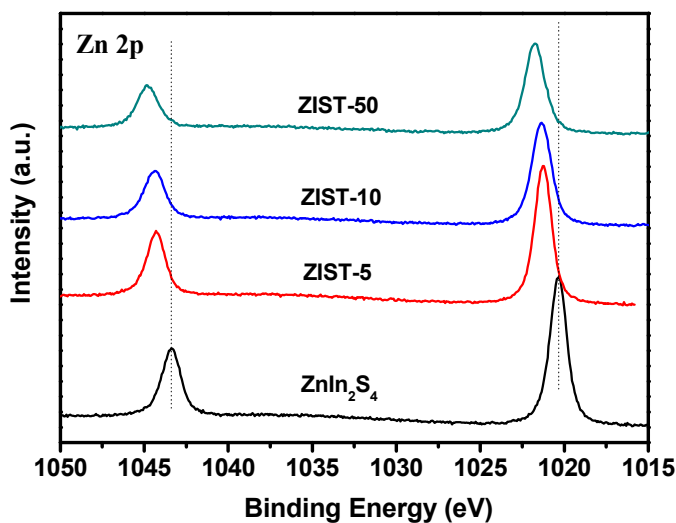


Figure 10. XPS Zn 2p spectra of ZnIn₂S₄ and ZnIn₂S₄/Ti₃C₂ composites with different Ti₃C₂ content.

DRS was used to measure the light harvesting capability of the photocatalyst samples. A clear red shift was exhibited for the $\text{ZnIn}_2\text{S}_4/\text{Ti}_3\text{C}_2$ nanocomposites, and their absorption in the visible light region was significantly enhanced compared with pure ZnIn_2S_4 (Figure 11). As the Ti_3C_2 content increased, the absorption intensity of $\text{ZnIn}_2\text{S}_4/\text{Ti}_3\text{C}_2$ gradually increased due to the full-spectrum absorption of dark Ti_3C_2 [23]. Because of the high efficiency of photothermal conversion of Ti_3C_2 [22], it is possible to activate the catalyst by converting the light energy into heat to promote the surface catalytic reaction [29].

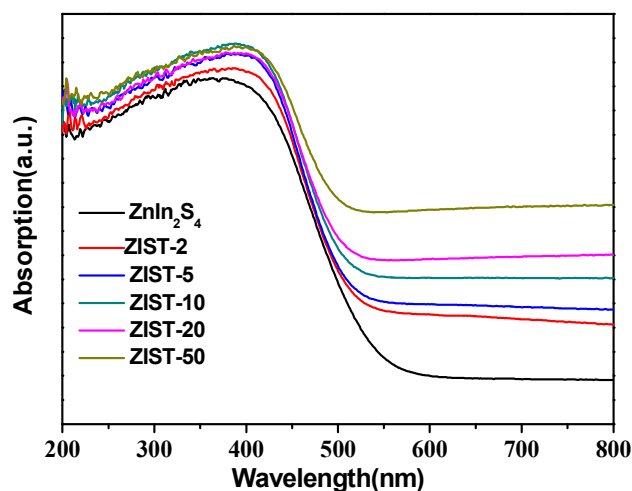


Figure 11. UV–vis DRS spectra of ZnIn_2S_4 and $\text{ZnIn}_2\text{S}_4/\text{Ti}_3\text{C}_2$ composites with different Ti_3C_2 content.

2.2. Photocatalytic Activity

The photocatalytic performance of the samples was measured according to the hydrogen evolution from water under visible light irradiation (>420 nm). As expected, a significant enhancement in the photocatalytic activity for hydrogen evolution was observed upon loading of a small amount of Ti_3C_2 (Figure 12). When the mass ratio of Ti_3C_2 reaches 5% (ZIST-5), the best photocatalytic activity is obtained ($2.6 \text{ mmol}\cdot\text{g}^{-1}\cdot\text{h}^{-1}$). However, with the further increase in Ti_3C_2 content, the photocatalytic activity gradually decreased. This may be due to an excess of Ti_3C_2 causing the composite materials to become too conductive. The result is the depression in charge separation efficiency over the composite [30]. In addition, the presence of Ti_3C_2 with a large amount of dark will also have a shading effect, which is not conducive to the light absorption of composite materials. In addition, the recyclability of ZIST-5 for photocatalytic hydrogen production was also evaluated. The cycling experiments show that the yield of hydrogen could still reach $2.4 \text{ mmol}\cdot\text{g}^{-1}\cdot\text{h}^{-1}$ after four cycles (Figure 13a). The XRD spectra show that the crystal structure of the recovered catalyst remains intact except for some weakening of crystallinity, indicating that it has excellent stability. For a comparison, the same proportions of Pt and graphene (5 wt.%) were loaded on ZnIn_2S_4 , respectively. Under the same experimental conditions, $\text{ZnIn}_2\text{S}_4/\text{Pt}$ and $\text{ZnIn}_2\text{S}_4/\text{graphene}$ showed lower photocatalytic activities of $1.3 \text{ mmol}\cdot\text{g}^{-1}\cdot\text{h}^{-1}$ and $1.0 \text{ mmol}\cdot\text{g}^{-1}\cdot\text{h}^{-1}$ than of ZIST-5, respectively (Figure 14). These results indicate that ZIST-5 is a promising photocatalyst for photocatalytic hydrogen production.

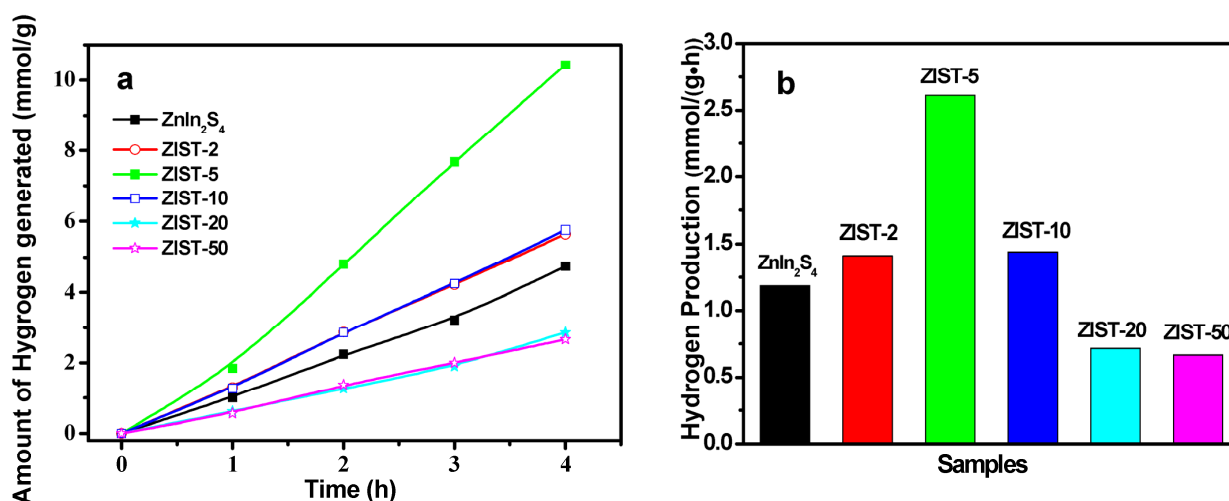


Figure 12. (a) Photocatalytic H₂ evolution over ZnIn₂S₄ and ZnIn₂S₄/Ti₃C₂ composites with different Ti₃C₂ content under visible light irradiation. (b) Rate of H₂ evolution of ZnIn₂S₄/Ti₃C₂ composites with different Ti₃C₂ content under visible light irradiation.

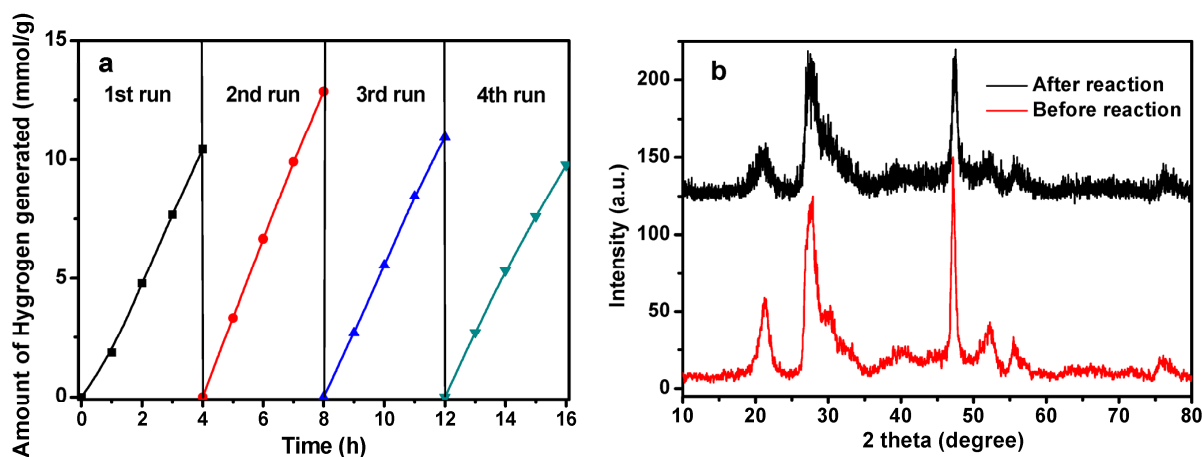


Figure 13. (a) Cycling tests of photocatalytic H₂ production under visible light irradiation over ZIST-5. (b) XRD patterns for experimental ZIST-5 before and after the reaction.

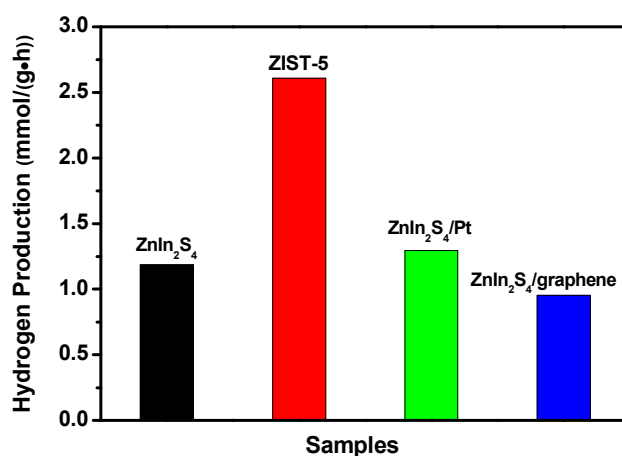


Figure 14. Rate of H₂ evolution of ZnIn₂S₄, ZnIn₂S₄/Pt, ZnIn₂S₄/graphene, and ZIST-5 under visible light irradiation.

3. Discussion

3.1. The Photoluminescence Spectra and Electrochemical Impedance Spectra

In order to further comprehend the role of Ti_3C_2 in improving the photocatalytic activity of ZnIn_2S_4 , the photoluminescence (PL) spectra and electrochemical impedance spectra (EIS) were recorded. PL emission is generated by the recombination of electrons and holes; therefore, lower PL intensity indicates higher separation efficiency of photo-generated electron-hole pairs [30]. As shown in Figure 15, the PL spectra show that the main emission peaks of ZnIn_2S_4 and ZIST-5 appear at 537 nm, while the intensity of the emission peak of ZIST-5 is much weaker than that of ZnIn_2S_4 . This suggests the heterogeneous junction formed between Ti_3C_2 and ZnIn_2S_4 can enhance the efficiency of photogenerated electron and hole separation. In photocurrent response spectra (Figure 16), ZIST-5 showed a higher photocurrent than ZnIn_2S_4 and, thus, more efficient separation and transportation of photoinduced charge carriers [31]. In the EIS Nyquist plot, a smaller arc radius indicates lower charge transfer resistance at the electrode surface and higher separation efficiency for electron-hole pairs [32]. In Figure 17, the arc radius of ZIST-5 is a little less than that of pure ZnIn_2S_4 in the darkness, suggesting that ZIST-5 has more effective separation of photogenerated charges. Under visible light irradiation, the arc radius of ZIST-5 and ZnIn_2S_4 significantly decreases compared with that of darkness, and ZIST-5 decreases more than that of ZnIn_2S_4 . These results show that in ZIST-5, Ti_3C_2 acts as an electron acceptor to capture photoelectrons produced by ZnIn_2S_4 due to its good electrical conductivity. Moreover, it can increase the photocatalytic activity by effectively inhibiting photoinduced carrier recombination.

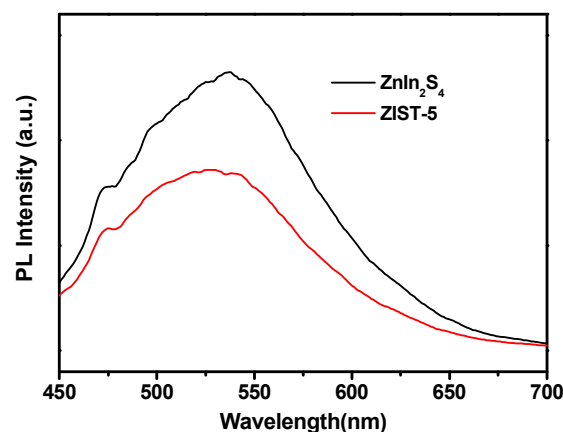


Figure 15. PL spectra of ZnIn_2S_4 and ZIST-5.

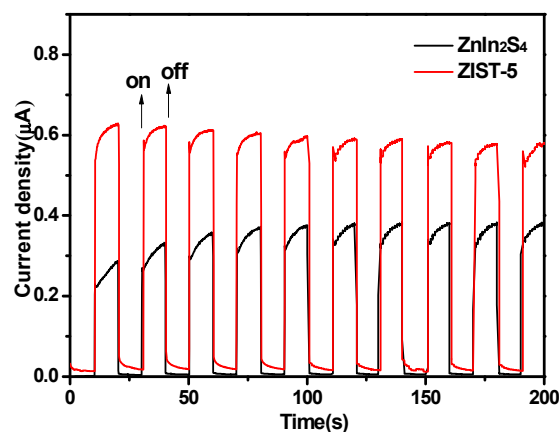


Figure 16. Transient photocurrent responses of ZnIn_2S_4 and ZIST-5 (300 W Xe lamp equipped with a 420 nm cut-off filter as a light source).

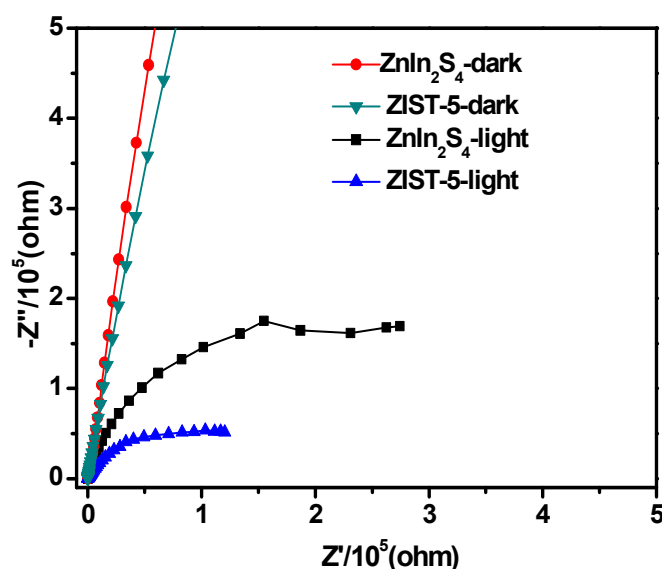
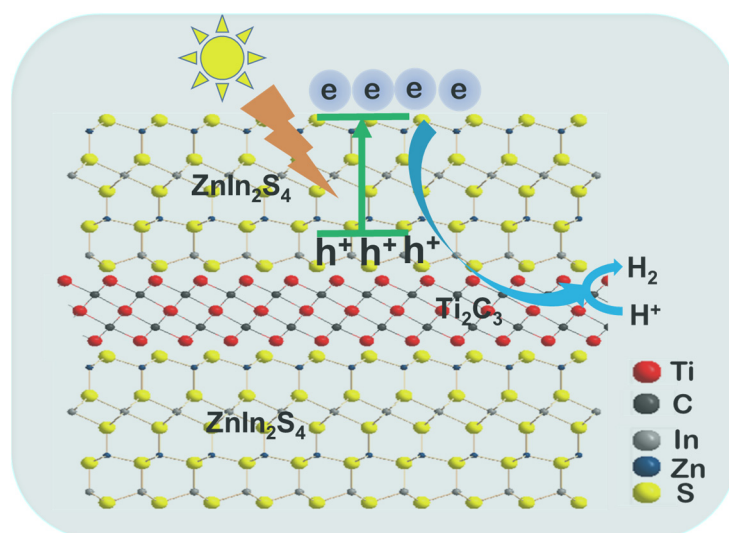


Figure 17. Nyquist plots of experimental impedance data for ZnIn_2S_4 and ZIST-5 in the frequency range of 4 MHz to 10 MHz using an AC bias of 0 V vs. Ag/AgCl without or with visible light irradiation ($\lambda > 420$ nm).

3.2. The Photocatalytic Mechanism

Based on the findings presented above, we propose the possible mechanism of the photocatalytic reaction for this system as shown in Scheme 1. Upon visible light irradiation, electrons (e^-) are excited from the valence band (VB) to the conduction band (CB) of the ZnIn_2S_4 semiconductor, creating holes (h^+) in the VB. Electrons are transferred to the Ti_3C_2 nanosheets and accumulate. These electrons can effectively reduce H_2O (or H^+) to produce H_2 , and the accumulated (h^+) in the VB of ZnIn_2S_4 react with $\text{S}^{2-}/\text{SO}_3^{2-}$ as a regenerative reagent. The presence of Ti_3C_2 can serve as an excellent electron acceptor and mediator, with effective separation of holes and electrons. This results in a significant improvement in the photocatalytic activity.



Scheme 1. Suggested mechanism for the photocatalysis of $\text{Ti}_2\text{C}_3/\text{ZnIn}_2\text{S}_4$ under visible light.

4. Materials and Methods

4.1. Synthesis of Samples

All reagents were of analytical grade and used without further purification. Ti_3AlC_2 powder (>98 wt.% purity) was purchased from Beijing Lianli New Technology Co., Ltd.,

Beijing, China. By etching the Al layer of Ti_3AlC_2 with HF solution, Ti_3C_2 was obtained. In brief, 1 g Ti_3AlC_2 powder was slowly combined with 30 mL HF solution (content ≥ 40 wt.%, Xilong Chemical Co., Ltd., Shantou, China), and the mixture was stirred at room temperature for 72 h. The suspension was filtered and washed with deionized water several times, until neutral pH was achieved. The obtained Ti_3C_2 was dried under vacuum at 60°C for 2 h.

Next, a hydrothermal reaction was employed to prepare the $\text{ZnIn}_2\text{S}_4/\text{Ti}_3\text{C}_2$ nanocomposites. An appropriate amount of Ti_3C_2 was dispersed in 70 mL of water by ultrasonication. To the Ti_3C_2 dispersion, ZnCl_2 (0.136 g, 1 mmol, Tianjin Fengchuan Chemical Reagent Technology Co. Ltd., Tianjing, China) and excess L-cysteine were added, and the mixture was ultrasonicated. Subsequently, $\text{InCl}_3\cdot 4\text{H}_2\text{O}$ (0.586 g, 2 mmol., Adamas Reagent Co. Ltd., Beijing, China) and thioacetamide (TAA, 0.300 g, 4 mmol., Sinopharm Chemical Reagent Co., Ltd., Shanghai, China) were added, and the solution was transferred to a 100 mL Teflon liner, sealed in a stainless steel autoclave, and heated at 150°C for 5 h. The product was collected by centrifugation, washed several times with de-ionized water, and dried under vacuum at 60°C for 12 h. The mass ratio of ZnIn_2S_4 to Ti_3C_2 was varied to determine the optimal composition, and mass ratios of 2 wt.%, 5 wt.%, 10 wt.%, 20 wt.%, and 50 wt.% corresponded to samples ZIST-2, ZIST-5, ZIST-10, ZIST-20, and ZIST-50, respectively.

4.2. Characterizations

Powder X-ray diffraction (XRD) data were collected using a Rigaku TTRAX III X-ray diffractometer (Rigaku D/max-3B, Tokyo, Japan) with $\text{Cu K}\alpha$ radiation. A field emission scanning electron microscope (SEM) (FEIQuanta200FEG microscope, FEI, Eindhoven, The Netherlands) was used to examine the morphology of the sample. Transmission electron microscopy (TEM) and high-resolution transmission electron microscopy (HRTEM) images were obtained on a JEM-2100 microscope (JEOL, Tokyo, Japan). X-ray photoelectron spectroscopy (XPS) was performed on a K-Alpha XPS system (Thermo Fisher Scientific, Waltham, MA, USA) with a monochromatic $\text{Al K}\alpha$ source. A Shimadzu UV-2600 photometer was used to record the UV-vis diffuse reflectance spectra (UV-vis DRS, Shimadzu, Kyoto, Japan), using BaSO_4 as a reflectance standard. A PGSTAT 302N electrochemical analyzer (Metrohm, Herisau, Switzerland) was used to record the photocurrent response spectra and electrochemical impedance spectra (EIS) in a standard three-electrode system. The prepared samples were used as the working electrodes with an active area of ca. 0.25 cm^2 on ITO conductive glass. Pt wire was the counter electrode, a standard calomel electrode was used as the reference electrode, and 0.5 M Na_2SO_4 aqueous solution was used as the electrolyte. A F-7000 fluorescence spectrophotometer (Hitachi, Tokyo, Japan) was used to record the photoluminescence (PL) spectra of powder samples at an excitation wavelength of 325 nm.

4.3. Photocatalytic H_2 Generation

Photocatalytic H_2 evolution experiments were conducted in a closed gas circulation and evacuation system fitted with a Pyrex glass window (LABSOLAR-H2I, Beijing Perfectlight Technology Co., Ltd., Beijing, China). In 100 mL of a mixed aqueous solution containing 0.05 M Na_2SO_3 (Xilong Scientific Co., Ltd., Shantou, China) and 0.05 M Na_2S (Xilong Scientific Co., Ltd., Shantou, China), 20 mg of photocatalyst was suspended, and the suspension was irradiated with a 300 W Xe lamp (CEL-HXF300, China Education Au-light Co. Ltd., Beijing, China) equipped with a 420 nm cut-off filter. Using a circulating water bath, the solution was maintained at room temperature during the reaction. The concentration of H_2 was directly detected by an on-line gas chromatograph (GC-9750, Chengdu Fuli Instrument Co., Ltd., Chengdu, China) equipped with a thermal conductivity detector (TCD).

5. Conclusions

In conclusion, a facile hydrothermal method was employed for the successful preparation of 2D/2D $\text{ZnIn}_2\text{S}_4/\text{Ti}_3\text{C}_2$ composite photocatalysts. The 2D/2D $\text{ZnIn}_2\text{S}_4/\text{Ti}_3\text{C}_2$

heterostructures showed excellent interface activity, ideal photoresponsivity properties, and high photogenerated carrier mobility. Our findings suggest Ti_3C_2 MXene has a unique synergistic effect on photocatalytic hydrogen production due to its unique two-dimensional structure, fast carrier migration rate, and ideal interfacial effect. The separation of photogenerated carriers and the transfer of photoelectrons to MXene nanosheets were significantly promoted by the incorporation of the heterojunction between ZnIn_2S_4 and Ti_3C_2 . As a result, we observed a significant improvement in the photocatalytic activity. This work provides a novel synthetic method for the preparation of 2D MXene composite photocatalytic materials and expands the utility of these materials to energy storage and conversion applications.

Author Contributions: Conceptualization, Y.C. and J.W.; methodology, Y.G.; validation, C.W. and H.T.; formal analysis, L.J. and X.L.; data curation, X.L.; writing—original draft preparation, Y.C.; writing—review and editing, Y.C. and J.H.; project administration, Z.Y.; funding acquisition, Y.C. and J.W. All authors have read and agreed to the published version of the manuscript.

Funding: This research was funded by the National Natural Science Foundation of China (21773204, 22062026, 22062024), Yunnan Applied Basic Research Projects (202201AS070003, 202101AT070017), and the Yunnan High-Level Talents Training Support Program (YNWR-QNBJ-2020-093, YNWR-YLXZ-2019-002).

Institutional Review Board Statement: Not applicable.

Informed Consent Statement: Not applicable.

Data Availability Statement: Data available on request.

Acknowledgments: The authors thank the Advanced Analysis and Measurement Center of Yunnan University for the sample characterization.

Conflicts of Interest: The authors declare no conflict of interest.

References

1. Fujishima, A.; Honda, K. Electrochemical Photolysis of Water at a Semiconductor Electrode. *Nature* **1972**, *238*, 37–38. [[CrossRef](#)]
2. Zhang, S.; Liu, Z.; Yan, W.; Guo, Z.; Ruan, M. Decorating non-noble metal plasmonic Al on a $\text{TiO}_2/\text{Cu}_2\text{O}$ photoanode to boost performance in photoelectrochemical water splitting. *Chin. J. Catal.* **2020**, *41*, 1884–1893. [[CrossRef](#)]
3. Liu, Z.; Wang, X. Efficient photoelectrochemical water splitting of $\text{CaBi}_6\text{O}_{10}$ decorated with Cu_2O and NiOOH for improved photogenerated carriers. *Int. J. Hydrogen Energy* **2018**, *43*, 13276–13283. [[CrossRef](#)]
4. Fang, G.; Liu, Z.; Han, C. Enhancing the PEC water splitting performance of BiVO_4 co-modifying with NiFeOOH and Co-Pi double layer cocatalysts. *Appl. Surf. Sci.* **2020**, *515*, 146095. [[CrossRef](#)]
5. Chen, Y.; Ge, H.; Wei, L.; Li, Z.; Yuan, R.; Liu, P.; Fu, X. Reduction degree of reduced graphene oxide (RGO) dependence of photocatalytic hydrogen evolution performance over RGO/ ZnIn_2S_4 nanocomposites. *Catal. Sci. Technol.* **2013**, *3*, 1712–1717. [[CrossRef](#)]
6. Wei, L.; Chen, Y.; Lin, Y.; Wu, H.; Yuan, R.; Li, Z. MoS_2 as non-noble-metal co-catalyst for photocatalytic hydrogen evolution over hexagonal ZnIn_2S_4 under visible light irradiations. *Appl. Catal. B* **2014**, *144*, 521–527. [[CrossRef](#)]
7. Shang, L.; Zhou, C.; Bian, T.; Yu, H.; Wu, L.-Z.; Tung, C.-H.; Zhang, T. Facile synthesis of hierarchical ZnIn_2S_4 submicrospheres composed of ultrathin mesoporous nanosheets as a highly efficient visible-light-driven photocatalyst for H_2 production. *J. Mater. Chem. A* **2013**, *1*, 4552–4558. [[CrossRef](#)]
8. Fang, F.; Chen, L.; Chen, Y.-B.; Wu, L.-M. Synthesis and Photocatalysis of ZnIn_2S_4 Nano/Micropeony. *J. Phys. Chem. C* **2010**, *114*, 2393–2397. [[CrossRef](#)]
9. Huang, J.; Cheuk, W.; Wu, Y.; Lee, F.S.C.; Ho, W. Template-free synthesis of ternary sulfides submicrospheres as visible light photocatalysts by ultrasonic spray pyrolysis. *Catal. Sci. Technol.* **2012**, *2*, 1825–1827. [[CrossRef](#)]
10. Chen, Z.; Li, D.; Zhang, W.; Chen, C.; Li, W.; Sun, M.; He, Y.; Fu, X. Low-Temperature and Template-Free Synthesis of ZnIn_2S_4 Microspheres. *Inorg. Chem.* **2008**, *47*, 9766–9772. [[CrossRef](#)]
11. Yang, M.-Q.; Xu, Y.-J.; Lu, W.; Zeng, K.; Zhu, H.; Xu, Q.-H.; Ho, G.W. Self-surface charge exfoliation and electrostatically coordinated 2D hetero-layered hybrids. *Nat. Commun.* **2017**, *8*, 14224. [[CrossRef](#)] [[PubMed](#)]
12. Shen, S.; Zhao, L.; Guo, L. Morphology, structure and photocatalytic performance of ZnIn_2S_4 synthesized via a solvothermal/hydrothermal route in different solvents. *J. Phys. Chem. Solids* **2008**, *69*, 2426–2432. [[CrossRef](#)]
13. Bai, X.; Li, J. Photocatalytic hydrogen generation over porous ZnIn_2S_4 microspheres synthesized via a CPBr-assisted hydrothermal method. *Mater. Res. Bull.* **2011**, *46*, 1028–1034. [[CrossRef](#)]
14. Shen, S.; Zhao, L.; Zhou, Z.; Guo, L. Enhanced Photocatalytic Hydrogen Evolution over Cu-Doped ZnIn_2S_4 under Visible Light Irradiation. *J. Phys. Chem. C* **2008**, *112*, 16148–16155. [[CrossRef](#)]

15. Shen, S.; Zhao, L.; Guan, X.; Guo, L. Improving visible-light photocatalytic activity for hydrogen evolution over ZnIn₂S₄: A case study of alkaline-earth metal doping. *J. Phys. Chem. Solids* **2012**, *73*, 79–83. [[CrossRef](#)]
16. Wang, Y.; Kong, X.; Jiang, M.; Zhang, F.; Lei, X. A Z-scheme ZnIn₂S₄/Nb₂O₅ nanocomposite: Constructed and used as an efficient bifunctional photocatalyst for H₂ evolution and oxidation of 5-hydroxymethylfurfural. *Inorg. Chem. Front.* **2020**, *7*, 437–446. [[CrossRef](#)]
17. Dang, X.; Xie, M.; Dai, F.; Guo, J.; Liu, J.; Lu, X. The in situ construction of ZnIn₂S₄/CdIn₂S₄ 2D/3D nano hetero-structure for an enhanced visible-light-driven hydrogen production. *J. Mater. Chem. A* **2021**, *9*, 14888–14896. [[CrossRef](#)]
18. Hao, M.; Deng, X.; Xu, L.; Li, Z. Noble metal Free MoS₂/ZnIn₂S₄ nanocomposite for acceptorless photocatalytic semi-dehydrogenation of 1,2,3,4-tetrahydroisoquinoline to produce 3,4-dihydroisoquinoline. *Appl. Catal. B* **2019**, *252*, 18–23. [[CrossRef](#)]
19. Zhao, Q.; Liu, Z.; Li, J.; Yan, W.; Ya, J.; Wu, X. Piezoelectric polarization assisted WO₃/CdS photoanode improved carrier separation efficiency via CdS phase regulation. *Int. J. Hydrogen Energy* **2021**, *46*, 36113–36123. [[CrossRef](#)]
20. Li, Y.; Liu, Z.; Li, J.; Ruan, M.; Guo, Z. An effective strategy of constructing a multi-junction structure by integrating a heterojunction and a homojunction to promote the charge separation and transfer efficiency of WO₃. *J. Mater. Chem. A* **2020**, *8*, 6256–6267. [[CrossRef](#)]
21. Zuo, G.; Wang, Y.; Teo, W.L.; Xie, A.; Guo, Y.; Dai, Y.; Zhou, W.; Jana, D.; Xian, Q.; Dong, W.; et al. Ultrathin ZnIn₂S₄ Nanosheets Anchored on Ti₃C₂TX MXene for Photocatalytic H₂ Evolution. *Angew. Chem. Int. Ed.* **2020**, *59*, 11287–11292. [[CrossRef](#)]
22. Cao, S.; Shen, B.; Tong, T.; Fu, J.; Yu, J. 2D/2D Heterojunction of Ultrathin MXene/Bi₂WO₆ Nanosheets for Improved Photocatalytic CO₂ Reduction. *Adv. Funct. Mater.* **2018**, *28*, 1800136. [[CrossRef](#)]
23. Su, T.; Hood, Z.D.; Naguib, M.; Bai, L.; Luo, S.; Rouleau, C.M.; Ivanov, I.N.; Ji, H.; Qin, Z.; Wu, Z. 2D/2D heterojunction of Ti₃C₂/g-C₃N₄ nanosheets for enhanced photocatalytic hydrogen evolution. *Nanoscale* **2019**, *11*, 8138–8149. [[CrossRef](#)]
24. Chen, Y.; Hu, S.; Liu, W.; Chen, X.; Wu, L.; Wang, X.; Liu, P.; Li, Z. Controlled syntheses of cubic and hexagonal ZnIn₂S₄ nanostructures with different visible-light photocatalytic performance. *Dalton Trans.* **2011**, *40*, 2607–2613. [[CrossRef](#)] [[PubMed](#)]
25. Li, Y.; Cai, J.; Hao, M.; Li, Z. Visible light initiated hydrothiolation of alkenes and alkynes over ZnIn₂S₄. *Green Chem.* **2019**, *21*, 2345–2351. [[CrossRef](#)]
26. Cai, T.; Wang, L.; Liu, Y.; Zhang, S.; Dong, W.; Chen, H.; Yi, X.; Yuan, J.; Xia, X.; Liu, C.; et al. Ag₃PO₄/Ti₃C₂ MXene interface materials as a Schottky catalyst with enhanced photocatalytic activities and anti-photocorrosion performance. *Appl. Catal. B* **2018**, *239*, 545–554. [[CrossRef](#)]
27. Chen, R.; Wang, P.; Chen, J.; Wang, C.; Ao, Y. Synergetic effect of MoS₂ and MXene on the enhanced H₂ evolution performance of CdS under visible light irradiation. *Appl. Surf. Sci.* **2019**, *473*, 11–19. [[CrossRef](#)]
28. Ran, J.; Gao, G.; Li, F.; Ma, T.; Du, A.; Qiao, S. Ti₃C₂ MXene co-catalyst on metal sulfide photo-absorbers for enhanced visible-light photocatalytic hydrogen production. *Nat. Commun.* **2017**, *8*, 13907. [[CrossRef](#)] [[PubMed](#)]
29. Lin, H.; Wang, X.; Yu, L.; Chen, Y.; Shi, J. Two-Dimensional Ultrathin MXene Ceramic Nanosheets for Photothermal Conversion. *Nano Lett.* **2017**, *17*, 384–391. [[CrossRef](#)] [[PubMed](#)]
30. Su, T.; Hood, Z.D.; Naguib, M.; Bai, L.; Luo, S.; Rouleau, C.M.; Ivanoy, I.N.; Ji, H.; Qin, Z.; Wu, Z. Monolayer Ti₃C₂Tx as an Effective Co-catalyst for Enhanced Photocatalytic Hydrogen Production over TiO₂. *ACS Appl. Energy Mater.* **2019**, *2*, 4640–4651. [[CrossRef](#)]
31. Zhang, S.; Liu, X.; Liu, C.; Luo, S.; Wang, L.; Cai, T.; Zeng, Y.; Yuan, J.; Dong, W.; Pei, Y.; et al. MoS₂ Quantum Dot Growth Induced by S Vacancies in a ZnIn₂S₄ Monolayer: Atomic-Level Heterostructure for Photocatalytic Hydrogen Production. *ACS Nano* **2018**, *12*, 751–758. [[CrossRef](#)] [[PubMed](#)]
32. Li, Y.; Yin, Z.; Ji, G.; Liang, Z.; Xue, Y.; Guo, Y.; Tian, J.; Wang, X.; Cui, H. 2D/2D/2D heterojunction of Ti₃C₂ MXene/MoS₂ nanosheets/TiO₂ nanosheets with exposed (001) facets toward enhanced photocatalytic hydrogen production activity. *Appl. Catal. B* **2019**, *246*, 12–20. [[CrossRef](#)]

Disclaimer/Publisher's Note: The statements, opinions and data contained in all publications are solely those of the individual author(s) and contributor(s) and not of MDPI and/or the editor(s). MDPI and/or the editor(s) disclaim responsibility for any injury to people or property resulting from any ideas, methods, instructions or products referred to in the content.